EPJ Web of Conferences **346**, 01025 (2026) https://doi.org/10.1051/epjconf/202634601025
RFPPC2025

MAPS: the MFEM Anisotropic Plasma Solver

Rhea Barnett[1,*], *Christina* Migliore[2], *Mark* Stowell[3], *Olena* Burkovska[1], *Ben* Dudson[3], *Jeremy* Lore[1], and *Cory* Hauck[1]

[1]Oak Ridge National Laboratory, Oak Ridge, TN, U. S. A
[2]Massachusetts Institute of Technology, Cambridge, MA, U. S. A
[3]Lawrence Livermore National Laboratory, Livermore, CA, U. S. A

Abstract. Simulating magnetically confined fusion plasmas presents a uniquely challenging problem due to the nonlinear anisotropic heat conduction. We introduce the MAPS (MFEM Anisotropic Plasma Solver) tool, which uses a high-order finite element method to compute transport solutions on unstructured meshes. We show results for a set of three 2-D verification tests, two of which demonstrate the expected convergence properties for various mesh resolutions and polynomial degrees. We then discuss the convergence rate for the third test.

1 Introduction

A new finite element fluid plasma transport solver is being developed to provide plasma solutions in the boundary of magnetic confinement devices near radio frequency (RF) actuators with high geometric fidelity. Heat conduction in a magnetized plasma is highly anisotropic due to the gyromotion of charged particles and the strong scaling of parallel conductivity with temperature. The numerical challenge of solving nonlinear anisotropic transport equations can be addressed by projecting them onto separate parallel and perpendicular (to the background magnetic field **B**) coordinates and using a mesh aligned with the magnetic field. However special treatment is then required at the boundaries where the grid intersects the plasma facing components (PFCs).

This is a particularly relevant challenge in the field of radio-frequency (RF) heating to understand how the RF power can affect plasma transport the far Scrape Off Layer (far-SOL). To investigate this phenomenon, we need to resolve the antenna and accurately describe far-SOL plasma transport, which requires a method to provide solutions on a combination of field aligned and geometry conforming meshes. Boundary plasma transport codes approach the far-SOL plasma calculations by using cut cells (e.g., EMC3 [1, 2], EDGE2D [3]), using unaligned cells in the far-SOL only (SOLPS-ITER extended grid [4], or flexible field aligned coordinates BOUT++ [5]).

An alternate approach is to employ a finite element solver. With appropriate preconditioning to avoid poor condition numbers, the finite element method is well suited to address this problem, as it can handle both structured and unstructured meshes, and has been demonstrated to handle anisotropic plasma transport with high order elements (e.g., SolEdge-HDG [6], M3D-C1 [7]). Here we present the MAPS (MFEM [8, 9] Anisotropic Plasma Solver) code, which implements a discontinuous Galerkin (DG) high order finite element method to solve nonlinear anisotropic heat conduction in 2D. Recent progress in developing a hybrid DG FEM plasma solver [6, 10–14] indicates that this approach is suitable for developing a tokamak SOL transport solver. As a first result, we present important verification tests of MAPS including multiple 2D benchmarks. The fluid transport model will be coupled with the cold plasma full-wave code Stix [15, 16], a frequency domain wave solver developed for the far-SOL and RF antenna region, including a non-linear sheath boundary condition. Coupling MAPS and Stix will self-consistently evaluate how RF waves and far-SOL plasma profiles can impact each other via RF sheath enhanced $\mathbf{E}\times\mathbf{B}$ flows [17–21] and the ponderomotive force [22–28].

2 General physics model

The physics model for MAPS is developed following a similar approach to codes like SOLPS-ITER [29, 30], EMC3-EIRENE, UEDGE [31], and EDGE2D [3]: plasma turbulence is not resolved; cross-field transport is represented with user-defined diffusivities; and **B** is considered static. Using the definitions $\mathbf{b} = \mathbf{B}/B$, $B = ||\mathbf{B}||$, $\nabla_{\parallel} = \mathbf{b}\cdot\nabla$, $\nabla_{\perp} = (\bar{\bar{\mathrm{I}}} - \mathbf{b}\mathbf{b})\cdot\nabla$, $\nabla f = \mathbf{b}\nabla_{\parallel} f + \nabla_{\perp} f$, we solve the following set of equations for a Braginskii-like model [32, 33] for continuity, ion parallel momentum, and both ion and electron total energies,

$$\frac{\partial}{\partial t} n + \nabla\cdot(n\mathbf{b}u_{\parallel} - D_{\perp}\nabla_{\perp} n) = S^{n}, \qquad (2.1)$$

*Corresponding author: barnettrl@ornl.gov This manuscript has been authored in part by UT-Battelle, LLC, under contract DE-AC05-00OR22725 with the US Department of Energy (DOE). The publisher acknowledges the US government license to provide public access under the DOE Public Access Plan (http://energy.gov/downloads/doe-public-access-plan).

 https://doi.org/10.1051/epjconf/202634601025

$$\frac{\partial}{\partial t}(m_i n u_\parallel) + \nabla \cdot (m_i n u_\parallel^2 \mathbf{b}) = \nabla \cdot (m_i u_\parallel D_\perp \nabla_\perp n)$$
$$+\nabla_\parallel (m_i n \mu_\parallel \nabla_\parallel u_\parallel) + \nabla \cdot (m_i n \mu_\perp \nabla_\perp u_\parallel)$$
$$- \nabla_\parallel [n(T_e + T_i)] + S_\parallel^m, \tag{2.2}$$

$$\frac{\partial}{\partial t}\left(\frac{3}{2} n T_e\right) + \nabla \cdot \left(\frac{5}{2} n T_e \mathbf{b} u_\parallel - \frac{5}{2} n T_e D_\perp \nabla_\perp n\right.$$
$$\left. - n\chi_{\parallel,e} \mathbf{b} \nabla_\parallel T_e - n\chi_{\perp,e} \nabla_\perp T_e\right) = \frac{3 m_e n \nu_e}{m_i}(T_e - T_i)$$
$$- enu_\parallel E_\parallel + eD_\perp \nabla_\perp n + S_e^E + S_e^{E,ext}, \tag{2.3}$$

$$\frac{\partial}{\partial t}\left(\frac{3}{2} n T_i + \frac{1}{2} m_i n u_\parallel^2\right) + \nabla \cdot \left[\left(\frac{5}{2} n T_i + \frac{1}{2} m_i n u_\parallel^2\right) \mathbf{b} u_\parallel\right]$$
$$- \nabla \cdot \left[\left(\frac{5}{2} n T_i + \frac{1}{2} m_i n u_\parallel^2\right)\left(\frac{1}{n} D_\perp \nabla_\perp n\right)\right]$$
$$+ \nabla \cdot (n\chi_{\parallel,i} \mathbf{b} \nabla_\parallel T_i - n\chi_{\perp,i} \nabla_\perp T_i)$$
$$+ \nabla \cdot (\bar{\bar{\pi}}_i \cdot \mathbf{b} u_\parallel)) - \nabla \cdot \bar{\bar{\pi}}_i \cdot \frac{1}{n} D_\perp \nabla_\perp n$$
$$= \frac{3 m_e n \nu_e}{m_i}(T_e - T_i) + enu_\parallel E_\parallel + S_i^E + S_i^{E,ext}, \tag{2.4}$$

where we assume quasi-neutrality and a single hydrogenic ion species such that $n_i = n_e = n$. The subscripts i, e refer to the ion and electron quantities. The $\perp, \parallel$ subscripts indicate values perpendicular and parallel to the background magnetic field: D, μ, and χ are the coefficients (m^2/s) for particle diffusion, viscosity, and heat diffusion for the density, momentum, and energy equations respectively, where the parallel components are calculated using the usual expressions (see e.g., [32]) and we use ad-hoc values for the cross field components; $\nu_{i,e}$ are the collision frequencies; the source terms, $S^{n,m,E}$, contain any contributions from plasma-neutral interactions; and $S_{i,e}^{E,ext}$ are the external heat sources (e.g., from RF heating). For simplicity in initial development and testing, cross-field drifts, impurity ions, and plasma currents are currently neglected. However, these can be included in further development.

The system of equations is nonlinear with multiple time and length scales, with regions of strong spatial and temporal gradients that may change in location during the course of the simulation. To meet these challenges we will make use of adaptive time stepping, and discuss adaptive mesh refinement (AMR) in Section 4.

3 Anisotropic diffusion in two dimensions

While the MAPS code currently includes the full set of equations given in Eqs 2.1–2.4, for initial benchmarking purposes we consider a subset of these equations focused on the anisotropic heat diffusion problem,

$$\frac{\partial}{\partial t}\left(\frac{3}{2} n T\right) + \nabla \cdot \mathbf{q} = Q, \tag{3.1}$$
$$\mathbf{q} = -[\chi_\perp (\bar{\bar{\mathbf{I}}} - \mathbf{bb}) + \chi_\parallel \mathbf{bb}] \cdot \nabla T \tag{3.2}$$

with constant n. Systems of partial differential equations of the type modeled in this project require a set of nested solution methods. First there is an ordinary differential equation (ODE) solver used to advance the solution in time. The ODE solver involves the solution of a nonlinear operator for which we employ a Newton solver. The Newton solver must invert a linear gradient operator which we approximate using an iterative linear solver. Finally, the iterative solver can be accelerated using a preconditioner to compute an approximate inverse. Each of these steps will be described below but first we will briefly describe the choice of spatial discretization.

3.1 Spatial Discretization

Equations 2.1 through 2.4 resemble the scalar advection-diffusion-reaction problem studied in [34]. In this modeling effort we make use of the symmetric interior penalty Galerkin (SIPG) method (Eq. 3.8 in [34]) for the diffusive terms and the local Lax Friedrichs flux for the advective terms. The SIPG scheme includes a tunable parameter, α, which provides control over the degree of upwinding that can be independently applied across each edge.

3.2 Time Integration

Time step selection can have broad impact on a transient simulation. Unnecessarily small time steps can incur significant computational costs and introduce large accumulated errors. Inordinately large time steps can increase computational costs by producing poorly conditioned linear systems; miss short timescale transient phenomena which may be significant; and cause stability issues inherent in advection dominated flows. We employ a Proportional-Integral-Derivative (PID) controller for selecting the time step. The approach has been studied in [35] for a coupled viscous flow and heat transfer systems and more fully in [36] and [37]. A PID controller adjusts a control variable, $c(t)$, in an attempt to maintain a process variable, $p(t)$, near some set point, s. The deviation from the set point is called the error, $e(t) \equiv s - p(t)$,

$$c(t) = k_P\, e(t) + \frac{k_I}{\Delta t} \int_0^t e(\tau) d\tau + \Delta t\, k_D \frac{de(t)}{dt}.$$

The three parameters are the gains for the proportional, integral, and derivative terms that define the PID controller (Δt is used only to produce unitless values for k_I and k_D). At each time step the process variable, $p(t)$, is measured and this is used to determine $\Delta c(t)$, the change in the control variable, $c(t)$. The integral gain k_I controls how aggressively the PID controller will attempt to restrict the error, $e(t)$, below some tolerance, the proportional gain k_P reduces or enhances the integral factor according to the current slope of the error, $\frac{de(t)}{dt}$, and the derivative gain k_D reduces or enhances the previous factors based on the second derivative of the error, $\frac{d^2 e(t)}{dt^2}$.

We can use the same techniques to control the error in a numerical simulation by using the logarithms of the timestep and relative error as the control and process variables, respectively. This leads to time step adjustments made according to

$$dt_{n+1} = \min(\theta_n, \theta_{max})dt_n,$$

where

$$\theta_n = \left(\frac{tol}{r_n}\right)^{k_I} \left(\frac{r_{n-1}}{r_n}\right)^{k_P} \left(\frac{r_{n-1}^2}{r_n r_{n-2}}\right)^{k_D},$$

with θ_{max} being a limiting factor, tol the desired error tolerance, and r_n an approximation to the relative error in the solution at time t_n.

A common means to approximate the relative error is to use the local truncation error estimate from the ODE solver

$$r_n = \max_i \left(\frac{|e_i|}{|u_i| + \eta}\right),$$

where $\vec{u}$ is the solution, $\vec{e}$ is the local truncation error estimate, and $\eta > 0$ is used to avoid division by zero.

To obtain these error estimates we use an Embedded Singly-Diagonally Implicit Runge-Kutta (SDIRK) method. This method simultaneously computes the approximate time derivative of the ODE using two different orders of accuracy. The difference between these two solutions approximates the local truncation error. A further advantage of SDIRK methods over other implicit Runge-Kutta methods is that they contain a single value on the diagonal of their Butcher table. This means that each sub-iteration uses the same fractional time step when constructing the linear system which greatly reduces the computational effort needed to build and solve the implicit portion of the ODE.

A simple backward Euler time integration method with a fixed time step is also available. This is mainly for testing purposes but there are also certain classes of problems where a fixed time step may be desirable.

The non-linear system presented to the ODE solver is addressed with a standard Newton solver. The solution of the global linearized system is produced using GMRES with a block diagonal preconditioner. The block preconditioners applied to the different equations in the system may be chosen differently. Options for these preconditioners include sparse direct solvers such as SuperLU(_Dist) [38], or MUMPS [39] as well as multigrid preconditioners from the *hypre* [40] library.

3.3 Benchmarks

3.3.1 NIMROD benchmark

A benchmark developed as part of the NIMROD code [41] tests anisotropic heat conduction at varying degrees of anisotropy, polynomial basis function degree p, and grid resolution. To test the convergence of MAPS, we solved Eq. 3.1 over a unit square domain $[0, 1]^2$, on a grid with $1/4 \le \Delta x \le 1/128$, $\Delta y = \Delta x$, and using $1 \le p \le 5$. We considered anisotropies relevant to the far-SOL plasma, $\chi_\parallel/\chi_\perp \in \{10^3, 10^6, 10^9\}$. We set $Q = A_1 \sin(\pi x)\sin(\pi y)$ with $A_1 = 2\pi^2$, which, if we assume $3n/2 = 1$ and $\chi_\perp = 1$ for simplicity, gives the exact solution

$$T_{exact} = A_0 + (1 - \exp[-A_1 t])\sin(\pi x)\sin(\pi y), \quad (3.3)$$

with $A_0 = 0$. For $\mathbf{B}(x, y) = \sin(\pi x)\cos(\pi y)\hat{\mathbf{x}} - \cos(\pi x)\sin(\pi y)\hat{\mathbf{y}}$, $\mathbf{B}\cdot\nabla T = 0$ so that the solution does not depend on $\chi_\parallel$, i.e., we set $\chi_\perp = 1.0$ in the numerical simulations such that the solution in an isotropic case is analogous to the anisotropic case [41]. A similar set of results were presented in [42], but given the extensive changes made to MAPS since this previous publication, we believed it appropriate to repeat the benchmark.

Figures 1(a) - (c) show the benchmark results for $\chi_\parallel/\chi_\perp \in \{10^3, 10^6, 10^9\}$, respectively. The black lines show the L^2 error between the exact and numerical solutions, where the markers indicate the polynomial degree. The dashed red lines indicate the expected error trend, given by $O(\Delta x^{(p+1)})$. We observe in Fig. 1 that MAPS exhibits satisfactory convergence.

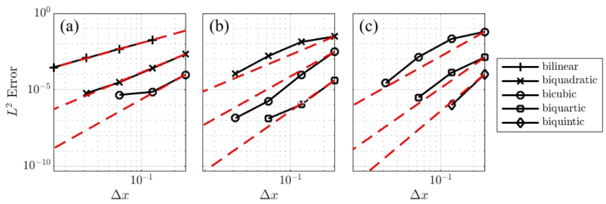

Figure 1. Results for (a) $\chi_\parallel/\chi_\perp = 10^3$, (b) $\chi_\parallel/\chi_\perp = 10^6$, and (c) $\chi_\parallel/\chi_\perp = 10^9$. The black lines indicate the L^2 error and the polynomial degree is indicated by the markers. The expected error trend, $O(\Delta x^{(p+1)})$, is shown with the red dashed lines.

3.3.2 Umansky benchmark

In addition to misalignment of the mesh to the magnetic field near the antenna and other PFCs, the solution can have strong spatial gradients. These occur around topological changes in the magnetic field (e.g., across the separatrix), and in the boundary layers that occur near PFCs. This is addressed using the verification test reported in [43]. Referring to Fig. 2, the magnetic field is aligned with the diagonal AC while the numerical mesh is not, and the degree of misalignment is given by $\tan\theta = (1.0/L)$ where L is the distance AB. This leads to a steady-state profile for T with a finite transition region described by the width w, defined as the distance between the contours $T = 0.25$ and $T = 0.75$ taken at $x = L/2$. As $\chi_\parallel/\chi_\perp \to \infty$, $w \to 0$. However, $w \ne 0$ for finite values of $\chi_\parallel/\chi_\perp$. As θ increases, w will broaden in the simulation compared with an "exact" solution. For the purpose of this benchmark, for the "exact" solution we compare with the semi-analytic solution derived in the Appendix of [43].

As in [43] we consider the domain $x \in [0, L]$, $y \in [0, 1]$ with the values $L = 1, 10, 100$, and Dirichlet boundary conditions $T(AD, DC) = 0$ and $T(AB, BC) = 1$. We set

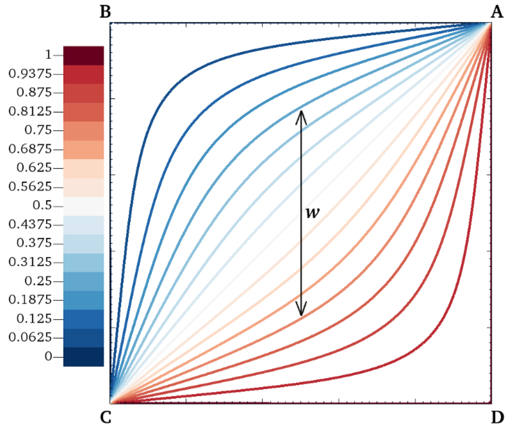

Figure 2. Solution for T_i with $L = 1$, $N = 40X40$, and $\chi_\parallel/\chi_\perp = 1.0$ at $t = 1.37$s. The boundary conditions are $T = 0$ on ABC and $T = 1$ on ADC, and the length $AB = L$ and $BC = 1$. The width is measured along w. Plotted with VisIt [44]

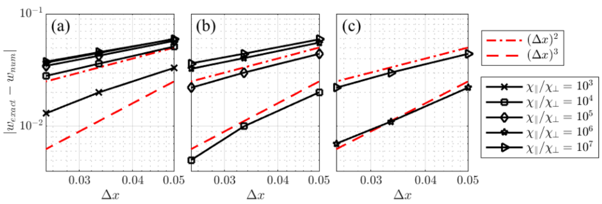

Figure 3. Absolute width error for (a) $L = 1$, (b) $L = 10$, and (c) $L = 100$. The markers indicate $\chi_\parallel/\chi_\perp$ values, with $\chi_\parallel/\chi_\perp < 10^3$ not included as it is not of interest. The dot dash and dash red lines correspond to errors $O(\Delta x)^2$ and $O(\Delta x)^3$ respectively. For cases not shown the error was either flat or equal to zero.

$p = 2$ and $N = 20X20$, $N = 30X30$, and $N = 40X40$ for N number of points. Figure 3 shows the absolute difference between the semi-analytic (w), and numerical (w_{num}) widths. For $p = 2$ we expect the convergence rate $O(\Delta x^2)$. Acceptable convergence is observed in Fig. 3(a) for all but the higher anisotropies at the larger pitch angle, which only show a small deviation from the expected trend.

3.3.3 Realistic magnetic field configuration

Here we use a single and double null magnetic field geometry to test a more realistic tokamak plasma scenario, based on the benchmark presented in [45]. Each benchmark solves Eq 3.1 over a unit square domain with $\chi_\parallel/\chi_\perp \in \{10^2, 10^4, 10^6\}$.

The single null magnetic flux profile is given by

$$A_z(\mathbf{x}) = \log(|\mathbf{x} - \mathbf{x_1}||\mathbf{x} - \mathbf{x_2}|), \qquad (3.4)$$

and the double null magnetic field flux profile is

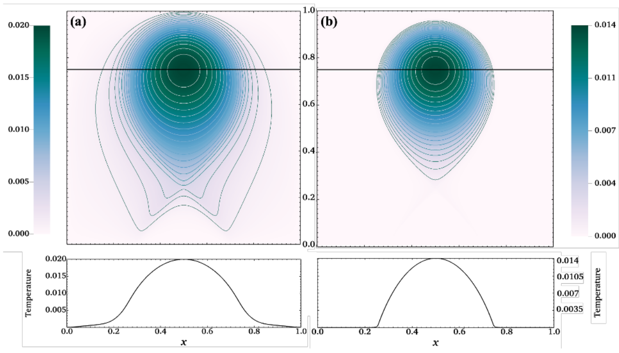

Figure 4. Reference temperature profiles for (a) $\chi_\parallel/\chi_\perp = 10^2$, and (b) $\chi_\parallel/\chi_\perp = 10^4$. The bottom figures are the corresponding 1D slices shown by the black line in each contour figure, illustrating how the resolution requirements change at the LCFS as the anisotropy increases.

$$A_z(x, y) = \frac{1}{2}(x - x_0)^2 + \frac{1}{2}\left[\frac{1}{4}\sin\left(2\pi(y - y_0)\right)\right]^2. \qquad (3.5)$$

We use the source term

$$Q(x, y, t) = \exp\left[-\frac{1}{2}\left(\left(\frac{x - 1/2}{1/8}\right)^2 + \left(\frac{y - 1/2}{1/8}\right)^2\right)\right] \qquad (3.6)$$

for both the single and double null cases. Additionally, $T(x, 0, t) = T(x, 1, t) = T(0, y, t) = T(1, y, t) = 0$, and $T(x, y, 0) = 0$. The poloidal magnetic field is then calculated by $\mathbf{B}_p = \nabla \times [A_z(x, y)\hat{\mathbf{z}}]$.

By including the source term within the last closed flux surface (LCFS), we observe the formation of a region of rapid temperature change of width $\propto \sqrt{\chi_\perp/\chi_\parallel}$ close to the separatrix [45]. The large temperature gradient in this region requires higher resolution to accurately capture as the anisotropy increases.

The single and double null benchmark results are shown in Figs. 5(a) and 5(b), respectively. The expected convergence rate is given by $O(\Delta x^{(p+1)})$ such that, with $p = 3$, we expect to observe a trend following $(\Delta x)^4$. For the single null case, we observe the L^2 error approaching the convergence for $\chi_\parallel/\chi_\perp \in \{10^2, 10^4\}$. However, for the double null case, the L^2 error approaches $O(\Delta x^3)$ as Δx is reduced. These results agree with the uniform refinement trend in Fig. 8 of [45]. We give a more in-depth discussion of these results in Section 4.

4 Conclusion and discussion

We have presented the MAPS code as a tool to solve anisotropic plasma diffusion problems of interest to magnetically confined fusion scenarios. The benchmark results in Figs 1 and 3 show that MAPS converges satisfactorily and can provide reliable solutions.

The results shown in Fig. 5 highlight the critical need for AMR that was originally reported in [45]: as the anisotropy increases, the temperature gradient increases at the LCFS (Fig. 4). When restricted to a uniformly spaced

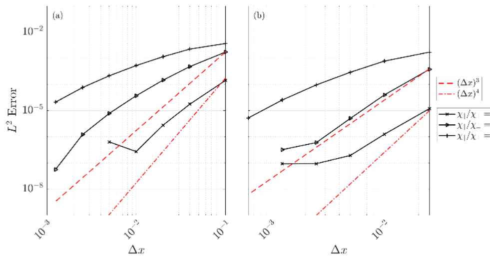

Figure 5. Black lines are the L^2 error for (a) the single null magnetic field, and (b) the double null magnetic field. The markers indicate different anisotropy ratios. The dash and dot dash red lines indicate orders of convergence $O(\Delta x^3)$ and $O(\Delta x^4)$ respectively.

grid, the DOFs required to resolve the boundary layer at $\chi_\parallel/\chi_\perp \in \{10^4, 10^6\}$ led to a problem that exceeded the available memory limits in the time-dependent solver: an additional steady state solver was developed to complement the MAPS code by computing the solutions at high anisotropy. The error floor observed in Fig. 5 can likely be explained by different tolerance definitions and thresholds between MAPS and the supplementary steady state solver. We next aim to include a preconditioner specialized for highly anisotropic problems [46] to relax the memory constraints.

Acknowledgments

This manuscript has been authored in part by UT-Battelle, LLC, with the US Department of Energy (DOE). The work was supported in part by the US DOE Office of Fusion Energy Sciences under contracts DE-AC05-00OR22725 and DE-AC52-07NA27344 as part of the SciDAC program. We would like to thank Christopher J. Vogl for the invaluable discussion with the realistic magnetic field configuration benchmark, John C. Wright and Syun'ichi Shiraiwa for their guidance as we navigated working with direct solvers, and Lin Mu for her continued help throughout.

References

[1] Y. Feng, F. Sardei, P. Grigull, K. McCormick, J. Kisslinger, D. Reiter, Y. Igitkhanov, Transport in island divertors: physics, 3D modelling and-comparison to first experiments on W7-AS, Plasma Physics and Controlled Fusion **44**, 611 (2002). https://doi.org/10.1088/0741-3335/44/5/308

[2] D. Reiter, M. Baelmans, P. Boerner, The EIRENE and B2-EIRENE codes, Fusion science and technology **47**, 172 (2005). https://doi.org/10.13182/FST47-172

[3] R. Simonini, G. Corrigan, G. Radford, J. Spence, A. Taroni, Models and Numerics in the Multi-Fluid 2-D Edge Plasma Code EDGE2D/U, Contributions to Plasma Physics **34**, 368 (1994). https://doi.org/10.1002/ctpp.2150340242

[4] W. Dekeyser, P. Boerner, S. Voskoboynikov, V. Rozhanksy, I. Senichenkov, L. Kaveeva, I. Veselova, E. Vekshina, X. Bonnin, R. Pitts et al., Plasma edge simulations including realistic wall geometry with SOLPS-ITER, Nuclear Materials and Energy **27**, 100999 (2021). https://doi.org/10.1016/j.nme.2021.100999

[5] J. Leddy, B. Dudson, M. Romanelli, B. Shanahan, N. Walkden, A novel flexible field-aligned coordinate system for tokamak edge plasma simulation, Computer Physics Communications **212**, 59 (2017). https://doi.org/10.1016/j.cpc.2016.10.009

[6] G. Piraccini, M. Capasso, M. Scotto D'Abusco, G. Giorgiani, F. Schwander, E. Serre, H. Bufferand, G. Ciraolo, P. Tamain, Recent upgrades in a 2D turbulent transport solver based on a hybrid discontinuous galerkin method for the simulation of fusion plasma in tokamak, Fluids **7**, 63 (2022). https://doi.org/10.3390/fluids7020063

[7] S.C. Jardin, A triangular finite element with first-derivative continuity applied to fusion mhd applications, Journal of Computational Physics **200**, 133 (2004). https://doi.org/10.1016/j.jcp.2004.04.004

[8] R. Anderson, J. Andrej, A. Barker, J. Bramwell, J.S. Camier, J. Cerveny, V. Dobrev, Y. Dudouit, A. Fisher, T. Kolev et al., MFEM: A modular finite element methods library, Computers & Mathematics with Applications **81**, 42 (2021). https://doi.org/10.1016/j.camwa.2020.06.009

[9] mfem, MFEM: Modular finite element methods [Software], `https://mfem.org`

[10] G. Giorgiani, H. Bufferand, G. Ciraolo, P. Ghendrih, F. Schwander, E. Serre, P. Tamain, A hybrid discontinuous Galerkin method for tokamak edge plasma simulations in global realistic geometry, Journal of Computational Physics **374**, 515 (2018). https://doi.org/10.1016/j.jcp.2018.07.028

[11] G. Giorgiani, H. Bufferand, G. Ciraolo, E. Serre, P. Tamain, A magnetic-field independent approach for strongly anisotropic equations arising in plasma-edge transport simulations, Nuclear Materials and Energy **19**, 340 (2019). https://doi.org/10.1016/j.nme.2019.03.002

[12] G. Giorgiani, H. Bufferand, F. Schwander, E. Serre, P. Tamain, A high-order non field-aligned approach for the discretization of strongly anisotropic diffusion operators in magnetic fusion, Computer Physics Communications **254**, 107375 (2020). https://doi.org/10.1016/j.cpc.2020.107375

[13] M.S. d'Abusco, G. Giorgiani, J.F. Artaud, H. Bufferand, G. Ciraolo, P. Ghendrih, E. Serre, P. Tamain, Core-edge 2D fluid modeling of full tokamak discharge with varying magnetic equilibrium: from WEST start-up to ramp-down, Nuclear Fusion **62**, 086002 (2022). https://doi.org/10.1088/1741-4326/ac47ad

[14] G. Piraccini, F. Schwander, E. Serre, G. Giorgiani, M. Scotto D'Abusco, Spatial adaptivity in SOLEDGE3X-HDG for edge plasma simulations in

versatile magnetic and reactor geometries, Contributions to Plasma Physics **62**, e202100185 (2022). https://doi.org/10.1002/ctpp.202100185

[15] C. Migliore, M. Stowell, J. Wright, P. Bonoli, Development of impedance sheath boundary condition in Stix finite element RF code, AIP Conference Proceedings **2984** (2023). https://doi.org/10.1063/5.0162402

[16] C. Migliore, J. Wright, M. Stowell, P. Bonoli, Using the Stix finite element RF code to investigate operation optimization of the ICRF antenna on Alcator C-Mod, Nuclear Fusion **63**, 106006 (2023). https://doi.org/10.1088/1741-4326/acee11

[17] M. Martin, W. Gekelman, B. Van Compernolle, P. Pribyl, T. Carter, Experimental observation of convective cell formation due to a fast wave antenna in the large plasma device, Physical Review Letters **119**, 205002 (2017). https://doi.org/10.1103/PhysRevLett.119.205002

[18] B. Van Compernolle, M. Martin, W. Gekelman, P. Pribyl, T. Carter, Fast wave experiments in LAPD in support of fusion, Preprint: Proc. 2018 IAEA Fusion Energy Conference, Gandhinagar [EX/P6-30] (2018).

[19] C. Lau, Y. Lin, G.R. Hanson, G. Wallace, S.J. Wukitch, B. LaBombard, R. Ochoukov, S. Shiraiwa, J. Terry, J. Wilgen, LH and ICRF driven scrape-off-layer density modifications and their impact on LH coupling on Alcator C-Mod, AIP Conference Proceedings **1580**, 410 (2014). https://doi.org/10.1063/1.4864575

[20] D. D'Ippolito, J. Myra, J. Jacquinot, M. Bures, Radio-frequency-sheath-driven edge plasma convection and interaction with the H mode, Physics of Fluids B: Plasma Physics **5**, 3603 (1993). https://doi.org/10.1063/1.860832

[21] W. Zhang, Y. Feng, J.M. Noterdaeme, V. Bobkov, L. Colas, D. Coster, T. Lunt, R. Bilato, J. Jacquot, R. Ochoukov et al., Modelling of the ICRF induced E× B convection in the scrape-off-layer of ASDEX Upgrade, Plasma Physics and Controlled Fusion **58**, 095005 (2016). https://doi.org/10.1088/0741-3335/58/9/095005

[22] W. Gekelman, R. Stenzel, Localized fields and density perturbations due to self-focusing of nonlinear lower-hybrid waves, Physical Review Letters **35**, 1708 (1975). https://doi.org/10.1103/PhysRevLett.35.1708

[23] G. Morales, Coupling of lower-hybrid radiation at the plasma edge, The Physics of Fluids **20**, 1164 (1977). https://doi.org/10.1063/1.861678

[24] V. Chan, S. Chiu, Wave-plasma coupling at the lower hybrid frequency, Phys. Fluids;(United States) **22** (1979). https://doi.org/10.1063/1.862808

[25] A. Fukuyama, T. Morishita, Y. Furutani, Nonlinear coupling of the slow wave structure with the lower-hybrid waves near the plasma surface, Plasma Phys. **22**, 565 (1980). https://doi.org/10.1088/0032-1028/22/6/006

[26] O. Meneghini, C. Lau, S. Shiraiwa, G.M. Wallace, R.R. Parker, B.L. LaBombard, I.C. Faust, J.R. Wilson, S.J. Wukitch, SOL Effects on LH Wave Coupling and Current Drive Performance on Alcator C-Mod, AIP Conference Proceedings **1406**, 411 (2011). https://doi.org/10.1063/1.3665004

[27] M. Preynas, M. Goniche, J. Hillairet, X. Litaudon, A. Ekedahl, L. Colas, Experimental characterization and modelling of non-linear coupling of the lower hybrid current drive power on Tore Supra, Nuclear Fusion **53**, 013012 (2013). https://doi.org/10.1088/0029-5515/53/1/013012

[28] R.L. Barnett, D.L. Green, C.L. Waters, J. Lore, D. Smithe, J.R. Myra, RF-transpond: A 1D coupled cold plasma wave and plasma transport model for ponderomotive force driven density modification parallel to B0, Computer Physics Communications **274**, 108286 (2022). https://doi.org/10.1016/j.cpc.2022.108286

[29] R. Schneider, X. Bonnin, K. Borrass, D. Coster, H. Kastelewicz, D. Reiter, V. Rozhansky, B. Braams, Plasma edge physics with B2-Eirene, Contributions to Plasma Physics **46**, 3 (2006). https://doi.org/10.1002/ctpp.200610001

[30] S. Wiesen, D. Reiter, V. Kotov, M. Baelmans, W. Dekeyser, A. Kukushkin, S. Lisgo, R. Pitts, V. Rozhansky, G. Saibene et al., The new SOLPS-ITER code package, Journal of nuclear materials **463**, 480 (2015). https://doi.org/10.1016/j.jnucmat.2014.10.012

[31] T. Rognlien, X. Xu, A. Hindmarsh, Application of parallel implicit methods to edge-plasma numerical simulations, Journal of Computational Physics **175**, 249 (2002). https://doi.org/10.1006/jcph.2001.6944

[32] S.I. Braginskii, Transport processes in a plasma, Reviews of Plasma Physics **1**, 205 (1965).

[33] E. Meier, U. Shumlak, A general nonlinear fluid model for reacting plasma-neutral mixtures, Physics of Plasmas **19** (2012). https://doi.org/10.1063/1.4736975

[34] B. Ayuso, L.D. Marini, Discontinuous Galerkin methods for advection-diffusion-reaction problems, SIAM Journal on Numerical Analysis **47**, 1391 (2009). https://doi.org/10.1137/080719583

[35] A. Valli, G. Carey, A. Coutinho, Control strategies for timestep selection in simulation of coupled viscous flow and heat transfer, Communications in Numerical Methods in Engineering **18**, 131 (2002). https://doi.org/10.1002/cnm.475

[36] K. Gustafsson, M. Lundh, G. Söderlind, A pi stepsize control for the numerical solution of ordinary differential equations, BIT Numerical Mathematics **28**, 270 (1988). https://doi.org/10.1007/BF01934091

[37] K. Gustafsson, Control-theoretic techniques for stepsize selection in implicit Runge-Kutta methods, ACM Transactions on Mathematical Software (TOMS) **20**, 496 (1994). https://doi.org/10.1145/198429.198437

[38] X.S. Li, J.W. Demmel, SuperLU_DIST: A scalable distributed-memory sparse direct solver for unsymmetric linear systems, ACM Transactions on Mathematical Software (TOMS) **29**, 110 (2003). https://doi.org/10.1145/779359.779361

[39] P.R. Amestoy, I.S. Duff, J.Y. L'Excellent, J. Koster, A fully asynchronous multifrontal solver using distributed dynamic scheduling, SIAM Journal on Matrix Analysis and Applications **23**, 15 (2001). https://doi.org/10.1137/S0895479899358194

[40] hypre, *hypre*: High performance preconditioners, `https://llnl.gov/casc/hypre`, `https://github.com/hypre-space/hypre`

[41] C. Sovinec, A. Glasser, T. Gianakon, D. Barnes, R. Nebel, S. Kruger, D. Schnack, S. Plimpton, A. Tarditi, M. Chu et al., Nonlinear magnetohydrodynamics simulation using high-order finite elements, Journal of Computational Physics **195**, 355 (2004). https://doi.org/10.1016/j.jcp.2003.10.004

[42] J.D. Lore, R.L. Barnett, D.L. Green, M.L. Stowell, M. Kobayashi, Development of a far-SOL unstructured-mesh fluid-plasma transport solver for RF antenna simulations, 28th IAEA Fusion Energy Conference (2021).

[43] M. Umansky, M. Day, T. Rognlien, On numerical solution of strongly anisotropic diffusion equation on misaligned grids, Numerical Heat Transfer, Part B: Fundamentals **47**, 533 (2005). https://doi.org/10.1080/10407790590928946

[44] H. Childs, E. Brugger, B. Whitlock, J. Meredith, S. Ahern, D. Pugmire, K. Biagas, M. Miller, C. Harrison, G.H. Weber et al., Visit: An end-user tool for visualizing and analyzing very large data, High Performance Visualization–Enabling Extreme-Scale Scientific Insight pp. 357–372 (2012). https://doi.org/10.1201/b12985

[45] C.J. Vogl, I. Joseph, M. Holec, Mesh refinement for anisotropic diffusion in magnetized plasmas, Computers & Mathematics with Applications **145**, 159 (2023). https://doi.org/10.1016/j.camwa.2023.06.019

[46] D. Green, X. Hu, J. Lore, L. Mu, M.L. Stowell, An efficient high-order solver for diffusion equations with strong anisotropy on non-anisotropy-aligned meshes, SIAM Journal on Scientific Computing **46**, S199 (2024). https://doi.org/10.1137/22M1500162